



Determining Dispersal Mechanisms of Protoplanetary Disks Using Accretion and Wind Mass Loss Rates

Yasuhiro Hasegawa¹, Thomas J. Haworth², Keri Hoadley³, Jinyoung Serena Kim^{4,5}, Hina Goto⁴, Aine Juzikenaite²,
Neal J. Turner¹, Iaria Pascucci^{6,5}, and Erika T. Hamden⁴

¹ Jet Propulsion Laboratory, California Institute of Technology, Pasadena, CA 91109, USA; yasuhiro.hasegawa@jpl.nasa.gov

² Astronomy Unit, School of Physics and Astronomy, Queen Mary University of London, London, E1 4NS, UK

³ Department of Physics & Astronomy, University of Iowa, 203 Van Allen Hall, Iowa City, IA 52242, USA

⁴ Steward Observatory, Department of Astronomy, University of Arizona, 933 North Cherry Avenue, Tucson, AZ 85721, USA

⁵ Alien Earths Team, NASA Nexus for Exoplanet System Science, USA

⁶ Lunar and Planetary Laboratory, University of Arizona, Tucson, AZ 85721, USA

Received 2021 December 6; revised 2022 January 28; accepted 2022 January 31; published 2022 February 21

Abstract

Understanding the origin of accretion and dispersal of protoplanetary disks is fundamental for investigating planet formation. Recent numerical simulations show that launching winds are unavoidable when disks undergo magnetically driven accretion and/or are exposed to external UV radiation. Observations also hint that disk winds are common. We explore how the resulting wind mass loss rate can be used as a probe of both disk accretion and dispersal. As a proof-of-concept study, we focus on magnetocentrifugal winds, magnetorotational instability turbulence, and external photoevaporation. By developing a simple yet physically motivated disk model and coupling it with simulation results available in the literature, we compute the wind mass loss rate as a function of external UV flux for each mechanism. We find that different mechanisms lead to different levels of mass loss rate, indicating that the origin of disk accretion and dispersal can be determined, by observing the wind mass loss rate resulting from each mechanism. This determination provides important implications for planet formation. This work thus shows that the ongoing and future observations of the wind mass loss rate for protoplanetary disks are paramount to reliably constrain how protoplanetary disks evolve with time and how planet formation takes place in the disks.

Unified Astronomy Thesaurus concepts: [Protoplanetary disks \(1300\)](#); [Circumstellar disks \(235\)](#); [Stellar accretion disks \(1579\)](#); [Magnetic fields \(994\)](#); [Magnetohydrodynamics \(1964\)](#); [Proplyds \(1296\)](#)

1. Introduction

Protoplanetary disks are widely accepted as the birth place of planetary systems and are known as highly dynamical objects; but how do they evolve with time? It is well established that once disks form and are isolated from their surrounding environments, disk evolution is caused by both mass accretion onto the host star and gas dispersal via launching winds from disk surfaces, if complexity arising from planet formation is neglected (e.g., Williams & Cieza 2011; Hartmann et al. 2016). One can therefore address this important question by identifying the dominant accretion and dispersal mechanisms in protoplanetary disks.

A number of mechanisms have been proposed in the literature (e.g., Turner et al. 2014; Ercolano & Pascucci 2017). Despite their variety, most mechanisms essentially assume that either magnetic fields threading through disks or heating by the host star and surrounding stars (or both) are responsible for disk accretion and dispersal. For the former, coupling magnetic fields with the disk gas leads not only to angular momentum transport/removal, but also to launching winds (e.g., Suzuki & Inutsuka 2009; Bai & Stone 2013). For the latter, heated gas gains the kinetic energy that fuel winds, especially in the outer disk, where the disk gas is less bound (e.g., Adams et al. 2004; Haworth & Clarke 2019). Recent observations infer the presence of magnetically driven winds originating from inner

($\lesssim 10$ au) disks (e.g., Fang et al. 2018; Whelan et al. 2021), and these winds may be launched at even larger disk radii (e.g., de Valon et al. 2020). Thus, it may be plausible to consider that disk accretion and dispersal occur mainly through three channels (Figure 1): mass accretion of disk gas onto its host star, inner magnetically driven winds, and outer thermal winds.

In this Letter, we adopt the above theoretically motivated and observationally supported picture of disk evolution, examining how the mass loss rate resulting from the inner/outer winds can serve as a useful probe of both disk accretion and dispersal mechanisms. Given that the inner and outer winds can be distinguished observationally (e.g., by launching locations or spectral features), we assume that the resulting mass loss rate is a local quantity computed from each wind. As a proof-of-concept study, we consider only magnetocentrifugal winds (MCWs), magnetorotational instability (MRI) turbulence, and external photoevaporation (EPE; Figure 1), where the latter becomes important when disks are exposed to sufficiently strong external UV fields. In this work, we do not include internal photoevaporation (Section 3). We show below that the wind mass loss rate arising from different mechanisms covers different parameter spaces. Therefore, we will conclude that the wind mass loss rate measured by observations can reveal the origin of disk accretion and dispersal in a wide range of star-forming regions.

2. Disk Accretion and Dispersal

The fundamental assumption of this work is that the ultimate origin of angular momentum transport/removal in protoplanetary



Original content from this work may be used under the terms of the [Creative Commons Attribution 4.0 licence](#). Any further distribution of this work must maintain attribution to the author(s) and the title of the work, journal citation and DOI.

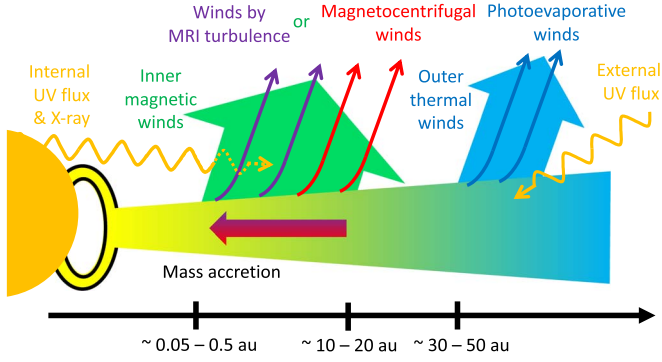


Figure 1. Schematic diagram of a protoplanetary disk and the wind mechanisms examined in this work. We consider only three channels (mass accretion, inner magnetic winds, and outer thermal winds) for disk accretion and dispersal; internal photoevaporation can be prevented due to the inner (massive) winds. The inner magnetic winds should be radially extended to reproduce the observed accretion rate.

disks are magnetic fields threading the disks, and that at least disk surfaces are ionized enough to couple with the fields due to radiation from the host star and/or external radiation.

2.1. Disk Model

We begin with the introduction of our disk model. The conservation of mass and angular momentum allows one to obtain the general, mathematical expression of the mass accretion rate onto the host star (\dot{M}_{acc} ; e.g., Balbus & Hawley 1998; Bai 2016; Suzuki et al. 2016). The expression assures decomposition of \dot{M}_{acc} into two components (e.g., Hasegawa et al. 2017):

$$\dot{M}_{\text{acc}} = \dot{M}_{\text{acc}}^{\text{Tur}} + \dot{M}_{\text{acc}}^{\text{DW}}, \quad (1)$$

where $\dot{M}_{\text{acc}}^{\text{Tur}}$ and $\dot{M}_{\text{acc}}^{\text{DW}}$ denote the contributions arising from MHD turbulence and disk winds, respectively. Many ideal and nonideal MHD simulations confirm that the accretion stress is dominated by the Maxwell stress, rather than the Reynold stress (e.g., Hawley et al. 1995; Bai & Stone 2013). Therefore, $\dot{M}_{\text{acc}}^{\text{Tur}}$ and $\dot{M}_{\text{acc}}^{\text{DW}}$ are specified once the strength and geometry of magnetic fields are determined.

When the α -prescription is used (Shakura & Sunyaev 1973), the effective viscosity (α_{SS}) mimicking disk turbulence is given as (e.g., Hasegawa et al. 2017)

$$\alpha_{\text{SS}} = \frac{1}{3\pi} \frac{\dot{M}_{\text{acc}}^{\text{Tur}}}{\Sigma_{\text{g}} H_{\text{g}}^2 \Omega}, \quad (2)$$

where $\Omega = \sqrt{GM_{\text{s}}/r^3}$ is the Keplerian, angular frequency around a host star with the mass of M_{s} , Σ_{g} the gas surface density, $H_{\text{g}} = c_{\text{s}}/\Omega$ the gas pressure scale height, and c_{s} the sound speed of the disk gas.

In the following, the above disk model is used to compute the mass loss rate, with $M_{\text{s}} = 1 M_{\odot}$, $H_{\text{g}}/r = h_0(r/1 \text{ au})^{1/4}$, and $h_0 = 0.05$.

2.2. Magnetocentrifugal Winds

The recent progress in nonideal MHD simulations suggests the importance of MCWs in protoplanetary disks (e.g., Turner et al. 2014); given that protoplanetary disks are generally dense and cold, MRI and the resulting MHD turbulence are likely

quenched in most regions (e.g., Gammie 1996; Wardle 2007). MCWs offer an alternative mechanism of disk accretion.

The primary origin of these winds is magnetocentrifugal force. The force becomes effective when disks are threaded by relatively strong, open magnetic fields that are suitably inclined from the polar axis; the differential rotation of Keplerian disks winds up the poloidal component of magnetic fields above the disk surfaces. These fields act like a lever arm anchored on the disk surfaces and can efficiently remove disks' angular momentum by launching winds.

The corresponding mass loss rate ($\dot{M}_{\text{loss}}^{\text{MCW}}$) is computed from the conservation of angular momentum (e.g., Bai et al. 2016):

$$\dot{M}_{\text{acc}}^{\text{DW}} \frac{dj}{dr} \Big|_{r_{\text{w}}} = \frac{d\dot{M}_{\text{loss}}^{\text{MCW}}}{dr} \Omega (r_{\text{A}}^2 - r_{\text{w}}^2), \quad (3)$$

where $j(r) \equiv \Omega r^2$ is the disks' specific angular momentum at r , r_{w} the wind-launching radius, and r_{A} the Alfvén radius. Note that $\dot{M}_{\text{loss}}^{\text{MCW}}$ is the *cumulative* mass loss rate from the wind-launching region, that is,

$$\dot{M}_{\text{loss}}^{\text{MCW}} = \int_{r_{\text{in}}}^{r_{\text{out}}} dr 2\pi r (\rho v)_{H_{\text{w}}}^{\text{MCW}}, \quad (4)$$

where r_{in} and r_{out} are the inner and outer boundaries of the region, and $(\rho v)_{H_{\text{w}}}^{\text{MCW}}$ are the gas density and velocity at the wind base with a height of H_{w} , respectively.

Equation (3) can be rewritten as

$$\xi(r_{\text{A}}/r_{\text{w}}) \equiv \frac{d\dot{M}_{\text{loss}}^{\text{MCW}}/d \ln r}{\dot{M}_{\text{acc}}^{\text{DW}}} \Big|_{r_{\text{w}}} = \frac{1}{2} \frac{1}{(r_{\text{A}}/r_{\text{w}})^2 - 1}, \quad (5)$$

which is referred to as the “ejection index” (Ferreira & Pelletier 1995). Also, $(r_{\text{A}}/r_{\text{w}})$ is often called the “magnetic lever arm.” This equation indicates that $r_{\text{A}}/r_{\text{w}} \geq \sqrt{3/2} \simeq 1.2$ since $\xi(r_{\text{A}}/r_{\text{w}}) \leq 1$.⁷ Based on the results of nonideal MHD simulations (Gressel et al. 2020), we adopt $r_{\text{A}}/r_{\text{w}} \simeq 1.6$ as an upper limit (see their Table 2).

Consequently, the mass loss rate due to MCWs is given as

$$\dot{M}_{\text{loss}}^{\text{MCW}} = \dot{M}_{\text{acc}}^{\text{DW}} \int_{r_{\text{in}}}^{r_{\text{out}}} dr \frac{\xi(r_{\text{A}}/r)}{r}. \quad (6)$$

2.3. Magnetorotational Instability Turbulence

MRI has been well recognized as the central engine of disk accretion because the instability surely grows in Keplerian disks (Balbus & Hawley 1991). As described above, however, its operation in protoplanetary disks has recently been challenged due to nonideal MHD effects, except for the vicinity of the host star. It is thus of fundamental importance to determine whether MRI-driven turbulence plays a dominant role in disk evolution.

The wind mass loss rate can be used as a tracer of MRI turbulence because ideal MHD simulations show that MRI turbulence can launch winds (Suzuki & Inutsuka 2009; see Miller & Stone 2000). The origin of winds is the generation of

⁷ Recent nonideal MHD simulations show that $r_{\text{A}}/r_{\text{w}}$ can become smaller than 1.2 (Bai 2017; Wang et al. 2019); in this case, the primary origin of launching winds is likely the magnetic pressure arising from the toroidal component. Given that such winds tend to be massive due to inefficient angular momentum removal, MCWs become more important for comparing with the MRI turbulence case (see Section 2.5).

large-scale channel flow in the vertical direction and its subsequent breakup due to magnetic reconnection around the disk surface. The reconnection converts magnetic energy to thermal energy (e.g., Sano & Inutsuka 2001), and hence the ultimate source of energy to launch winds is the gravitational energy released by the accretion stress, phenomenologically the viscous heating (Suzuki et al. 2016).⁸

The energy available for winds can be constrained from the conservation law (Suzuki et al. 2016). The resulting constraint leads to the condition that $0 \leq 1/\xi \leq 1$; equivalently, $1 \leq r_A/r_w \leq \sqrt{3/2} \simeq 1.2$ (see Appendix A for the mathematical derivation). This condition ensures that MRI turbulence and MCWs are mutually exclusive.

A tighter constraint is obtained by MHD simulations; Suzuki et al. (2010) show that $(\rho v)_{H_w}^{\text{MRI}}/(\rho_{\text{mid}} c_s)$ is linearly proportional to α_{SS} broadly, where $\rho_{\text{mid}} = \Sigma_g/(\sqrt{2\pi} H_g)$ is the gas density at the midplane (see their Figure 2). This linear relation is the direct reflection that winds are launched due to the accretion energy and allows one to explicitly define the energy loss (E_w^{MRI}) caused by winds due to MRI turbulence as (see Appendix A)

$$E_w^{\text{MRI}} \equiv \frac{r^2 \Omega^2}{2} (\rho v)_{H_w}^{\text{MRI}} = \frac{\epsilon}{(2\pi)^{3/2}} \frac{\dot{M}_{\text{acc}}^{\text{Tur}}}{H_g^2} r^2 \Omega^2, \quad (7)$$

where ϵ is the proportionality constant determined by MHD simulations. Then, the energy partition coefficient (η) of the accretion energy between winds and radiation is given as

$$\eta(\epsilon, r) \equiv \frac{E_w^{\text{MRI}}}{3\Omega^2 \dot{M}_{\text{acc}}^{\text{Tur}}/(4\pi)} = \frac{\epsilon}{3\sqrt{2\pi}} \left(\frac{r}{H_g} \right)^2. \quad (8)$$

Based on the simulation results of Suzuki & Inutsuka (2009), $\alpha = 0.012$ and $(\rho v)_{H_w}^{\text{MRI}}/(\rho_{\text{mid}} c_s) \simeq 8 \times 10^{-5}$ at the plasma $\beta = 10^6$ with $\sqrt{2} H_g/r = 0.1$. This leads to $\eta(\epsilon \simeq 7 \times 10^{-3}, r) \simeq 0.18$, suggesting that about 18% of the accretion energy is used to launch winds. Note that this estimate should be an upper limit; the simulations adopt the shearing box approximation, and the isothermal assumption is employed, both of which increases $(\rho v)_{H_w}^{\text{MRI}}$. We therefore consider that the following may be a reasonable upper limit: $\eta = 0.1$; or, equivalently, $\epsilon \simeq 2 \times 10^{-3}$ at $r = 1$ au.

As a result, the wind mass loss rate due to MRI turbulence is written as (see Equations (7) and (8))

$$\begin{aligned} \dot{M}_{\text{loss}}^{\text{MRI}} &= \int_{r_{\text{in}}}^{r_{\text{out}}} dr 2\pi r (\rho v)_{H_w}^{\text{MRI}} \\ &= \int_{r_{\text{in}}}^{r_{\text{out}}} dr \dot{M}_{\text{acc}}^{\text{Tur}} \frac{3\eta(\epsilon, r)}{r} = \frac{\dot{M}_{\text{acc}}^{\text{Tur}}}{\sqrt{2\pi}} \int_{r_{\text{in}}}^{r_{\text{out}}} dr \frac{\epsilon}{r} \left(\frac{r}{H_g} \right)^2. \end{aligned} \quad (9)$$

2.4. External Photoevaporation

Massive stellar clusters host OB stars that emit strong UV radiation. If the UV field incident upon a disk is sufficiently high, it can drive winds from the outer disk (e.g., Richling &

Yorke 2000; Haworth & Clarke 2019). The process is known as EPE and contributes to disk dispersal significantly.

We compute external photoevaporative mass loss rates ($\dot{M}_{\text{loss}}^{\text{EPE}}$) by utilizing the FRIED grid (Haworth et al. 2018). FRIED is built upon the results of radiation hydrodynamic models and provides the mass loss rate as a function of the stellar mass (M_s), the disk mass (M_d) and radius (r_d), and external far-UV (FUV) flux (F_{FUV}).⁹ Previous studies show that $\dot{M}_{\text{loss}}^{\text{EPE}}$ is a strong function of r_d , more easily stripping material from the outer (less bound) regions of large disks (e.g., Adams et al. 2004). When the mass loss rate is higher than the rate of viscous spreading, the disk is truncated (e.g., Clarke 2007). This occurs rapidly until the disk is shrunk to a radius at which $\dot{M}_{\text{loss}}^{\text{EPE}}$ becomes comparable to \dot{M}_{acc} (Winter et al. 2020a; also see Appendix B for mathematical confirmation). Thus, $\dot{M}_{\text{loss}}^{\text{EPE}} \geq \dot{M}_{\text{acc}}$ for disks undergoing accretion. Note that EPE does not transport/remove disks' angular momentum, and hence accretion should be driven by magnetic fields as in Sections 2.2 and 2.3. This suggests that disks may exhibit both the inner magnetic and outer thermal winds simultaneously.

We compile the FRIED grid to find out the maximum value of $\dot{M}_{\text{loss}}^{\text{EPE}}$ as functions of r_d and F_{FUV} . As discussed below, our focus is on the ratio of the wind mass loss rate to the stellar accretion rate. We therefore convert M_d to \dot{M}_{acc} , using the observed correlation between M_d and \dot{M}_{acc} (Manara et al. 2019):

$$\log \left(\frac{\dot{M}_{\text{acc}}}{M_{\odot} \text{ yr}^{-1}} \right) = (0.9 \pm 0.1) \log \left(\frac{M_d}{M_{\odot}} \right) - (6.5 \pm 0.4). \quad (10)$$

Note that this correlation is derived originally from the dust disk mass (not the gas disk mass). Conversion from the dust to gas mass is done with the assumption that the gas-to-dust ratio is 100. Also, the observed data are obtained from objects in Chameleon I and Lupus, which both reside in low-UV environments; the estimated value of \dot{M}_{acc} becomes smaller for objects in high-UV environments, because disks in such environments are fully or partially truncated by EPE and hence are less massive. This trend is indeed confirmed by Rosotti et al. (2017, see their Figure 7). We, however, use the correlation because the counterpart in high-UV environments is not available in the literature currently; our estimate should be viewed as a conservative one.

Figure 2 shows the resulting, maximum value of $\dot{M}_{\text{loss}}^{\text{EPE}}/\dot{M}_{\text{acc}}$. As expected, the ratio becomes higher for larger r_d , and disk truncation (that is, $\dot{M}_{\text{loss}}^{\text{EPE}}/\dot{M}_{\text{acc}} \simeq 1$) occurs for smaller-sized disks with stronger F_{FUV} .

In the following, we use Figure 2 to compare $\dot{M}_{\text{loss}}^{\text{EPE}}/\dot{M}_{\text{acc}}$ with other dispersal mechanisms.

2.5. Comparison

We now determine whether the wind mass loss rate can be used as a probe of the accretion and dispersal mechanisms for protoplanetary disks. To directly compare the various dispersal

⁸ The operation of this mechanism is confirmed even when ohmic resistivity is included (Suzuki et al. 2010); the presence of MRI-active surface layers leads to the production and breakup of large-scale channel flow around disk surfaces.

⁹ This work adopts plausible ranges of M_d and r_d used in FRIED (i.e., $10^{-3} \leq M_d/M_{\odot} \leq 10^{-1}$ and $30 \text{ au} \leq r_d \leq 400 \text{ au}$; see Appendix C for a parameter study). Also, F_{FUV} is in units of G_0 , where $1 G_0 = 1.6 \times 10^{-3} \text{ erg cm}^{-2} \text{ s}^{-1}$ is the flux integrated over the range from 6 to 13.6 eV (Habing 1968). The background F_{FUV} is about 1 G_0 in the solar neighborhood.

Table 1
The Ratio of the Wind Mass Loss Rate to the Stellar Accretion Rate for Each Mechanism

Origin	Parameter	Ratio
Magnetocentrifugal winds (MCW)	$1.2 \lesssim r_A/r \lesssim 1.6$ ($0.32 \lesssim \xi \lesssim 1$)	$0.74 \lesssim \dot{M}_{\text{loss}}^{\text{MCW}}/\dot{M}_{\text{acc}}^{\text{MCW}} \lesssim 2.3$
MRI turbulence (MRI)	$\epsilon \leq 2 \times 10^{-3}$ ($\eta \leq 0.1$ at $r = 1$ au)	$\dot{M}_{\text{loss}}^{\text{MRI}}/\dot{M}_{\text{acc}}^{\text{MRI}} \lesssim 0.44$
External photoevaporation (EPE)	Figure 2	$1 \lesssim \dot{M}_{\text{loss}}^{\text{EPE}}/\dot{M}_{\text{acc}}^{\text{EPE}} \lesssim 600$

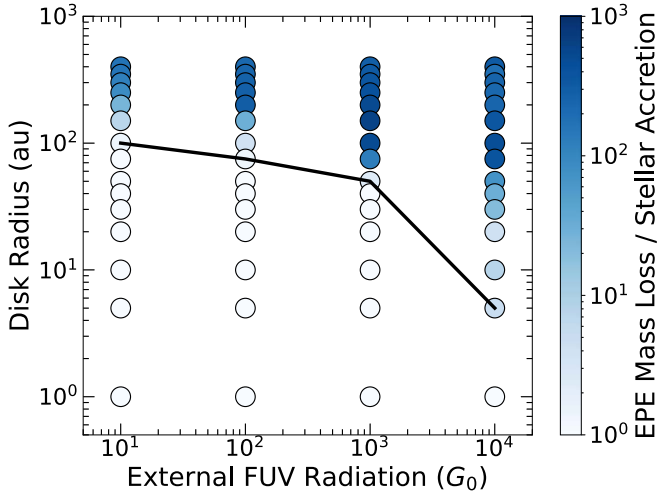


Figure 2. The maximum value of the ratio between external photoevaporative mass loss rates and stellar accretion rates. The FRIED grid is used to estimate the mass loss rate, and the observed correlation is used to convert the disk mass to the stellar accretion rate. The ratio is an increasing function of disk radius and external far-UV radiation. The black solid line defines the region where the ratio becomes larger than unity; below the line, disks are considered to have been already truncated by external photoevaporation.

mechanisms discussed above, we compute the ratio ($\dot{M}_{\text{loss}}/\dot{M}_{\text{acc}}$), under the assumption that in each case only the corresponding mechanism plays the dominant role for both \dot{M}_{acc} and \dot{M}_{loss} . We constrain the parameter space in which each mechanism becomes most important, by specifying the upper and lower limits of $\dot{M}_{\text{loss}}/\dot{M}_{\text{acc}}$.

Table 1 summarizes the results. For the MCW and MRI cases, we set that $r_{\text{in}} = 1$ au and $r_{\text{out}} = 10$ au, following recent observations (e.g., Fang et al. 2018; Louvet et al. 2018; Whelan et al. 2021). These choices are intended to examine how two kinds of inner, magnetically driven winds are differentiated by observations, and do not necessarily mean that the winds should be launched only in the region. For the EPE case, the widest range is picked in Table 1 for reference purposes, which is achieved at $10^3 G_0$ (see Figure 2).

Figure 3 shows the synthesized results. We find that the inner magnetic winds (i.e., MCW and MRI) play the major role in a disk's angular momentum transport/removal in low-UV environments, and their resulting mass loss can be observed at $F_{\text{FUV}} \lesssim 5 \times 10^3 G_0$; beyond this value, EPE truncates disks so much that the wind-launching region disappears (see the yellow shaded region). It is important that the MCW and MRI cases occupy different parameter space. Our results therefore indicate that if the corresponding mass loss and accretion rates are measured accurately enough, the origin of angular momentum transport/removal is determined. Note that time variability of mass loss rates may also be used to differentiate two kinds of inner magnetic winds (e.g., Suzuki et al. 2010).

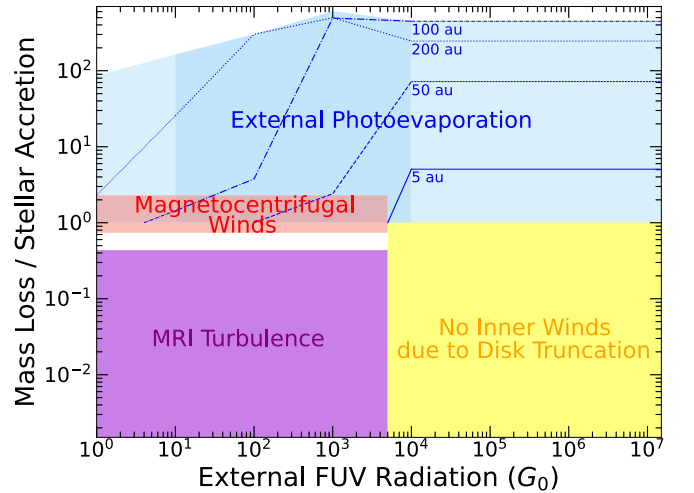


Figure 3. The ratio of the wind mass loss rate to the stellar accretion rate as a function of the external UV flux (also see Table 1 and Figure 2). The MCW case is denoted by the red shaded region, the MRI case the purple shaded region, and the EPE case the blue shaded region. For the EPE case, the disk radius dependence is explicitly denoted by the lines. The parameter space that is not covered by the current FRIED grid is denoted by the light blue shaded regions. Two inner magnetic winds can be differentiated by measuring the resulting mass loss rate, and the outer thermal winds and the resulting mass loss rate can be constrained by observing the disk radius.

For the EPE case, the current FRIED grid covers only from $10 G_0$ to $10^4 G_0$, and we extrapolate the results toward $1 G_0$ and put a limit for $>10^4 G_0$ (see the light blue shaded regions); both are reasonable because in lower-UV environments, the effect of photoevaporation becomes weaker, while in very-high-UV environments, disk truncation occurs very rapidly. The latter is indeed confirmed in Figure 3; the value of $\dot{M}_{\text{loss}}^{\text{EPE}}$ with $r_d = 100$ au becomes higher than that with $r_d = 200$ au at $F_{\text{FUV}} > 10^3 G_0$ because truncation is already in process for larger disks. We find that the resulting mass loss rate becomes very sensitive to the disk radius, as expected.

In summary, the mass loss rate resulting from inner magnetic winds can be used to determine the origin of angular momentum transport/removal and hence the dynamical properties (turbulent versus laminar) of the disk gas. This is the fundamental information for constraining how planets form in the disks (see Section 3). The mass loss rate originating from outer thermal winds is a sensitive function of the disk radius. Most of the disk mass is distributed in the outer part of the disk, and hence EPE regulates the formation timescale of planets and their final mass.

3. Discussion

This work has so far considered a specific set of parameters. We have conducted a parameter study and confirmed that the variation of parameters does not affect our findings significantly (see Appendix C); the MRI-dominated region can extend and

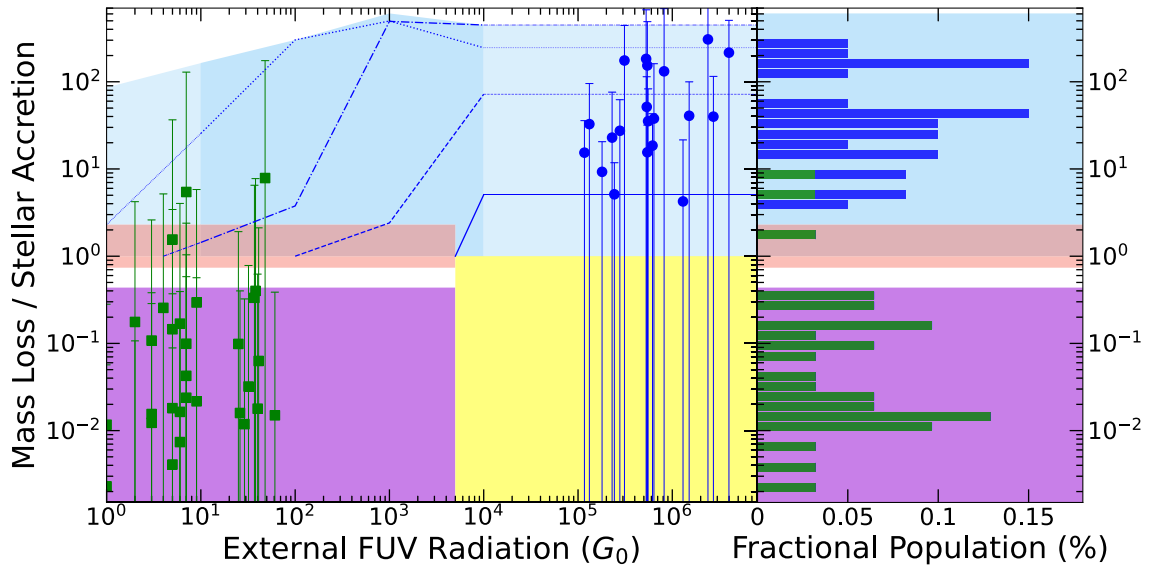


Figure 4. The distribution of the data currently available in the literature and the fractional population in the left and right panels, respectively. The observed systems are summarized in Tables 4 and 5 (denoted by the green and blue points, respectively), and the error estimation is described in Appendices D and E. The current, large uncertainties prevent one from determining the dominant accretion and dispersal mechanisms, while the data already show some structure, distributed mainly in the MRI and EPE regions.

overlap with the MCW one (that is, the empty space in Figure 3 may disappear). However, the parameter space specified in Figure 3 well represents the population of certain types of winds, and hence differentiating the origin of disk winds in the parameter space is possible, by observing a good number of disks. Our model has also assumed that disk surfaces are ionized enough to couple with magnetic fields, which is a requisite both for MCWs and MRI. The ionization structure of disks is poorly understood. The presence of (massive) inner winds may prevent the host star’s photons from reaching the disk surface and ionizing it (Pascucci et al. 2020), while external heating (e.g., cosmic rays) may be important for disk ionization (Seifert et al. 2021). Recent observations suggest that MRI is unlikely to operate at the surface of some disks (Flaherty et al. 2020), which may be used to constrain disk ionization. Finally, we have assumed that photoevaporation occurs only via external UV radiation. This is based on recent observations, which propose that the presence of inner (massive) winds can shield high-energy radiation from the host stars and suppress internal photoevaporation (Pascucci et al. 2020; see Figure 1). More observations are obviously needed to verify (or falsify) this picture; if internal photoevaporation drives winds, the corresponding mass loss rate should be comparable to that of MRI. Identifying the wind-launching region may allow one to differentiate these two winds.

Measuring the wind mass loss rate of protoplanetary disks provides a number of important implications for planet formation. The current observations are not accurate enough due to large uncertainties (Figure 4). However, the ongoing and future observations will improve accuracy. The most impactful implication of such observations is that they can constrain the mechanism of angular momentum transport/removal in protoplanetary disks. It is one fundamental parameter needed in planet formation models at all the stages: dust growth is limited by disk turbulence, especially in the inner-disk region (e.g., Birnstiel et al. 2012); planetesimal dynamics and growth are very sensitive to disk turbulence (e.g., Ida et al. 2008); the formation of planetary cores by pebble accretion is a function of the disk turbulence (e.g., Chambers 2016); and the behavior

of planetary migration can be drastically altered by the level of disk turbulence (e.g., McNally et al. 2019). Cumulatively, the resulting population of planets may differ significantly (e.g., Speedie et al. 2021). Note that when nonideal MHD effects quench MHD turbulence, hydrodynamical instabilities come into play to excite hydrodynamical turbulence in disks (Lyra & Umurhan 2019).

Another important implication is that measuring the mass loss rate in different UV environments allows one to explore when EPE plays a defining role in disk evolution and planet formation. This will provide new insights about how sensitive planet formation is to the surrounding environments, and shed light on the origin of the diversity of observed exoplanetary systems (e.g., Concha-Ramírez et al. 2019; Winter et al. 2020b).

In conclusion, observing wind mass loss rates of protoplanetary disks in a wide range of star-forming regions provides a key diagnostic of disk accretion and dispersal mechanisms. Conducting such observations is one critical step to better understand how protoplanetary disks evolve with time and how planet formation takes place in the disks.

The authors thank the referee, Giovanni Picogna, for the useful comments on the manuscript. The research was carried out at the Jet Propulsion Laboratory, California Institute of Technology, under a contract with the National Aeronautics and Space Administration (80NM0018D0004). Y.H. is supported by JPL/Caltech.

Appendix A

The Energy Budget for Winds Due to MRI Turbulence

The conservation of energy constrains the energy available for winds due to MRI turbulence (Suzuki et al. 2016):

$$\left(E_w + \frac{r^2 \Omega^2}{2} \right) (\rho v_z)_{H_w} + F_{\text{rad}} \Big|_{-H_w}^{H_w} = \frac{\Omega^2}{4\pi} (3\dot{M}_{\text{acc}}^{\text{Tur}} + \dot{M}_{\text{acc}}^{\text{DW}}), \quad (\text{A1})$$

where E_w is the energy needed to launch winds and F_{rad} is the energy loss due to radiation. According to Suzuki et al. (2016), we assume that $E_w = 0$, which is the minimum requirement. In addition, the following amount of energy is carried away by MCWs (see Equation (5)):

$$\frac{\Omega^2}{4\pi} \dot{M}_{\text{acc}}^{\text{DW}} = \frac{1}{\xi(r_A/r)} \frac{r^2 \Omega^2}{2} (\rho v_z)_{H_w}^{\text{MCW}}. \quad (\text{A2})$$

In other words, the energy loss (E_w^{MRI}) caused by winds due to MRI turbulence should have the range of, in the limit that $F_{\text{rad}} = 0$,

$$\left[1 - \frac{1}{\xi(r_A/r)} \right] \frac{r^2 \Omega^2}{2} (\rho v_z)_{H_w} \leq E_w^{\text{MRI}} \leq \frac{r^2 \Omega^2}{2} (\rho v_z)_{H_w}. \quad (\text{A3})$$

The above equation indicates that the necessary condition is $0 \leq 1/\xi \leq 1$; or, equivalently, $1 \leq r_A/r_w \leq \sqrt{3/2} \simeq 1.2$.

Thus, it is guaranteed that MRI turbulence and MCWs are mutually exclusive in terms of the magnetic lever arm. Note that the above range of E_w^{MRI} should be viewed as an upper bound due to the limit that $F_{\text{rad}} = 0$.

Appendix B

The Mass Loss Rate for Disks Truncated by External Photoevaporation

Efficient EPE truncates protoplanetary disks when the disks are exposed to high external UV radiation for long enough. For this case, the wind mass loss rate is controlled by viscous spreading if disk accretion is driven by viscosity; even when disks are already truncated, viscous spreading expands their sizes, and some gas is moved to the region where EPE is effective. Winter et al. (2020a) already explored this phenomenon in detail. We here provide a brief mathematical confirmation.

The mass loss rate ($\dot{M}_{\text{loss,tru}}^{\text{EPE}}$) for disks truncated by EPE is given as

$$\dot{M}_{\text{loss,tru}}^{\text{EPE}} = \zeta(r_t) \dot{M}_{\text{acc}}^{\text{Tur}}, \quad (\text{B1})$$

where r_t is the outer edge of the truncated disks:

$$\zeta(r_t) \equiv \frac{2(2+p)}{t_{\text{age}}/t_{\text{vis}}(r_t) + 1} - 1, \quad (\text{B2})$$

where p is the power-law index of $\Sigma_g (\propto r^p)$, t_{age} is the age of the system, and $t_{\text{vis}}(r_t)$ is the local viscous timescale at $r = r_t$. Note that r_t is automatically determined once the value of F_{FUV} is specified. We have used the similarity solution to obtain the functional form of $\zeta(r)$ (e.g., Hartmann et al. 1998), which is derived from the conservation of angular momentum under the assumption that disks' angular momentum is transported by effective viscosity (ν).

Given that the lifetime of truncated disks becomes comparable to $t_{\text{vis}}(r_t)$, and the FRIED grid adopts that $p = -1$ (Haworth et al. 2018), $\zeta(r_t)$ can be rewritten as

$$\zeta(r_t) \simeq \begin{cases} 1 & \text{for } t_{\text{age}} \lesssim t_{\text{vis}}(r_t), \\ 0 & \text{for } t_{\text{age}} \gtrsim t_{\text{vis}}(r_t), \end{cases} \quad (\text{B3})$$

where $t_{\text{vis}}(r_t)$ is given as

$$t_{\text{vis}}(r_t) = \frac{r_t^2}{3\nu(r_t)} = \frac{M_d(r_t)}{2\dot{M}_{\text{acc}}^{\text{Tur}}}. \quad (\text{B4})$$

Thus, the mass loss rate becomes comparable to $\dot{M}_{\text{acc}}^{\text{Tur}}$ when $t_{\text{age}} \lesssim t_{\text{vis}}(r_t)$, and no mass loss is produced from disks that have $t_{\text{age}} \gtrsim t_{\text{vis}}(r_t)$ as the disks already disperse.

One may wonder what is the origin of viscosity at the outer edge of truncated disks. While it is still poorly constrained, (at least) two possibilities can be considered: MRI and hydrodynamical turbulence. Note that MCW cannot play such a role as MHD turbulence is quenched due to nonideal MHD effects. If MRI operates both in the inner disk and at the outer edge, then the mass loss rate from inner winds is regulated by MRI. If MRI or hydrodynamical turbulence operates at the outer edge, but if MCW operates in the inner disk, then the mass loss rate from inner winds is controlled by MCW. This is because the contribution coming from MRI at the outer edge should be negligible (see Appendix C). Also, the mass loss rate from outer winds is always dominated by EPE because $\dot{M}_{\text{loss,tru}}^{\text{EPE}} \simeq \dot{M}_{\text{acc}}^{\text{Tur}}$ and $\dot{M}_{\text{loss,tru}}^{\text{MRI}} < \dot{M}_{\text{acc}}^{\text{Tur}}$.

Appendix C

Monte-Carlo-based Population Synthesis Calculations

We conduct a parameter study to explore the effect of variation of model parameters on our results (e.g., Figure 3). To proceed, we use the Monte-Carlo approach and generate disk populations. In the approach, the values of model parameters are chosen randomly with assumed distributions. The resulting value of $\dot{M}_{\text{loss}}/\dot{M}_{\text{acc}}$ is computed, using a set of these parameters. As shown below, the variation of model parameters does not change our conclusion significantly.

We first describe the range and distribution of model parameters adopted in this work. For inner magnetic winds, four parameters ($[r_A/r, r_{\text{in}}, r_{\text{out}}, h_0]$ and $[\epsilon, r_{\text{in}}, r_{\text{out}}, h_0]$) need to be specified both in the MCW and MRI cases, respectively (Table 2). Note that the dependence of M_s is explored effectively by changing h_0 in our model. The range of the parameters is chosen based on recent theoretical and observational studies (e.g., Figure 1 and Sections 2.2 and 2.3). Given that the true underlying distribution is unknown, we adopt a uniform distribution in linear space for four parameters ($r_A/r, r_{\text{in}}, r_{\text{out}}, h_0$) and a uniform distribution in logarithmical space for one parameter (ϵ); for the latter, logarithmical space is used to equally cover a larger parameter space in Figure 5. We consider that this is a conservative choice as all the plausible values of parameters are examined.

For outer thermal winds, four parameters ($M_s, G_0, r_d,$ and M_d) need to be selected (Table 3). As with the case for inner winds, the range of parameters is picked according to recent theoretical and observational studies (see Figure 1 and Section 2.4), and distributions are chosen to explore all the possible values of parameters. It should be noted that the ranges are constrained by the original FRIED grid, as well (Haworth et al. 2018). Using these parameters, realization of disk populations is conducted 1000 times for each case. The value of F_{FUV} is chosen such that disk populations are distributed uniformly in logarithmic space.

We then discuss the resulting disk populations. Figure 5 shows the results for inner magnetic winds. In order to elucidate the effect of each parameter, we consider six cases in total (Table 2).

Table 2
Sets of Model Parameters for Inner Magnetic Winds

	Magnetic Lever Arm		Proportionality Constant		Inner Boundary		Outer Boundary		Aspect Ratio	
	r_A/r		ϵ		r_{in} (au)		r_{out} (au)		h_0	
	Range	Distribution	Range	Distribution	Range	Distribution	Range	Distribution	Range	Distribution
Case 1 (Fiducial)	1.2–1.6	Linearly uniform	10^{-5} – 2×10^{-3}	Logarithmically uniform	1		10		0.05	
Case 2	1.2–1.6	Linearly uniform	10^{-5} – 2×10^{-3}	Logarithmically uniform	0.05–1	Linearly uniform	5–20	Linearly uniform	0.05	
Case 2a	1.2–1.6	Linearly uniform	10^{-5} – 2×10^{-3}	Logarithmically uniform	1		5–20	Linearly uniform	0.05	
Case 3	1.2–1.6	Linearly uniform	10^{-5} – 2×10^{-3}	Logarithmically uniform	1		10		0.01–0.1	Linearly uniform
Case 3a	1.2–1.6	Linearly uniform	10^{-5} – 2×10^{-3}	Logarithmically uniform	1		10		0.05–0.1	Linearly uniform
Case 4	1.2–1.6	Linearly uniform	10^{-5} – 2×10^{-3}	Logarithmically uniform	0.05–1	Linearly uniform	5–20	Linearly uniform	0.01–0.1	Linearly uniform

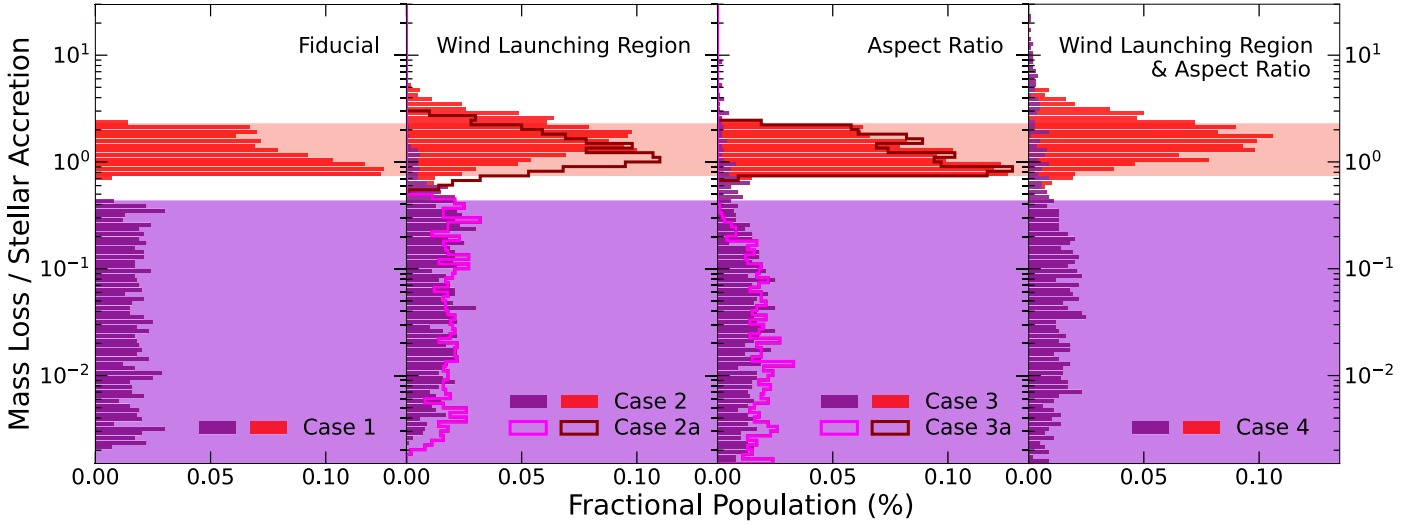


Figure 5. Disk populations for inner magnetic winds. The populations are generated by the Monte-Carlo approach (Table 2). In Case 1, only the values of r_A/r and ϵ vary. In Cases 2 and 2a, those of r_{in} and r_{out} change in addition to the values of r_A/r and ϵ . In Cases 3 and 3a, the effect of variation of h_0 is examined. In Case 4, all the parameters are altered. The variation of parameters leads to two overlapping populations (i.e., MCW and MRI). However, the overlap can be disentangled, by observing a sufficient number of disks.

Table 3
Sets of Model Parameters for Outer Thermal Winds

	Stellar Mass $M_* (M_\odot)$	External FUV Radiation $F_{FUV} (G_0)$	Disk Radius		Disk Mass	
			Range	Distribution	Range	Distribution
Case 5	0.5	1, 10, 10^2 , 10^3 , 10^4	30–400	Linearly uniform	10^{-3} – 10^{-1}	Logarithmically uniform
Case 5a	0.5	1, 10, 10^2 , 10^3 , 10^4	30–50	Linearly uniform	10^{-3} – 10^{-1}	Logarithmically uniform
Case 5b	0.5	1, 10, 10^2 , 10^3 , 10^4	30–400	Linearly uniform	10^{-3} – 10^{-2}	Logarithmically uniform
Case 6	1	1, 10, 10^2 , 10^3 , 10^4	30–400	Linearly uniform	10^{-3} – 10^{-1}	Logarithmically uniform
Case 6a	1	1, 10, 10^2 , 10^3 , 10^4	30–50	Linearly uniform	10^{-3} – 10^{-1}	Logarithmically uniform
Case 6b	1	1, 10, 10^2 , 10^3 , 10^4	30–400	Linearly uniform	10^{-3} – 10^{-2}	Logarithmically uniform
Case 7	1.6	1, 10, 10^2 , 10^3 , 10^4	30–400	Linearly uniform	10^{-3} – 10^{-1}	Logarithmically uniform
Case 7a	1.6	1, 10, 10^2 , 10^3 , 10^4	30–50	Linearly uniform	10^{-3} – 10^{-1}	Logarithmically uniform
Case 7b	1.6	1, 10, 10^2 , 10^3 , 10^4	30–400	Linearly uniform	10^{-3} – 10^{-2}	Logarithmically uniform

Case 1 explores the variation of only r_A/r , r_{in} and ϵ . As expected, most disks are located in the shaded regions; since the value of ϵ is sampled uniformly in logarithmical space, the resulting population becomes flat for the MRI case, which is beneficial for examining the effect of other parameters.

Case 2 examines how the variation of wind-launching regions affects disk populations. Our results show that both the populations spread vertically and the two cases (MCW and MRI) overlap. This overlap originates mainly from the choice of the inner boundary of wind-launching regions; when smaller r_{in} is picked (see Case 2), launching massive winds becomes possible due to a high density at the wind base for the MRI case. In fact, such a diffuse population disappears when $r_{in} = 1$ au (see Case 2a). However, the diffuse population for the MRI case is not large enough, compared with the population for the MCW case. This suggests that if a sufficient number of disks is observed, distinction between the MCW and MRI cases is possible.

Case 3 studies the effect of h_0 . We confirm a similar trend, that while the populations between the MCW and MRI cases overlap due to massive winds launched from low latitudes (i.e., low h_0 ; see Case 3a), the resulting overlap can be differentiated.

In Case 4, all the parameters vary. The corresponding population for the MRI case further extends toward higher values of $\dot{M}_{loss}/\dot{M}_{acc}$. However, such a population is minor compared with the MCW case.

In summary, it can be concluded that the shaded regions defined in Figure 3 are reasonable for purposes of demonstration in the proof-of-concept study; and even if the variation of model parameters is taken into account, differentiation between the MCW and MRI cases is possible, by observing a good number of disks exhibiting winds.

Figure 6 shows the results for outer thermal winds. In our preliminary efforts, we have found that some random combinations of two parameters (r_d and M_d) can lead to unrealistically high values of $\dot{M}_{loss}/\dot{M}_{acc}$. It can be written as

$$\frac{\dot{M}_{loss}}{\dot{M}_{acc}} = \frac{\dot{M}_{loss}}{M_d} \frac{M_d}{\dot{M}_{acc}} \equiv \frac{\tau_{acc}}{\tau_{loss}}, \quad (C1)$$

and hence such high values come from very small values of τ_{loss} . Given that the disk lifetime should be determined by $\min(\tau_{acc}, \tau_{loss})$, we cut off the value of τ_{loss} smaller than 10^6 yr.

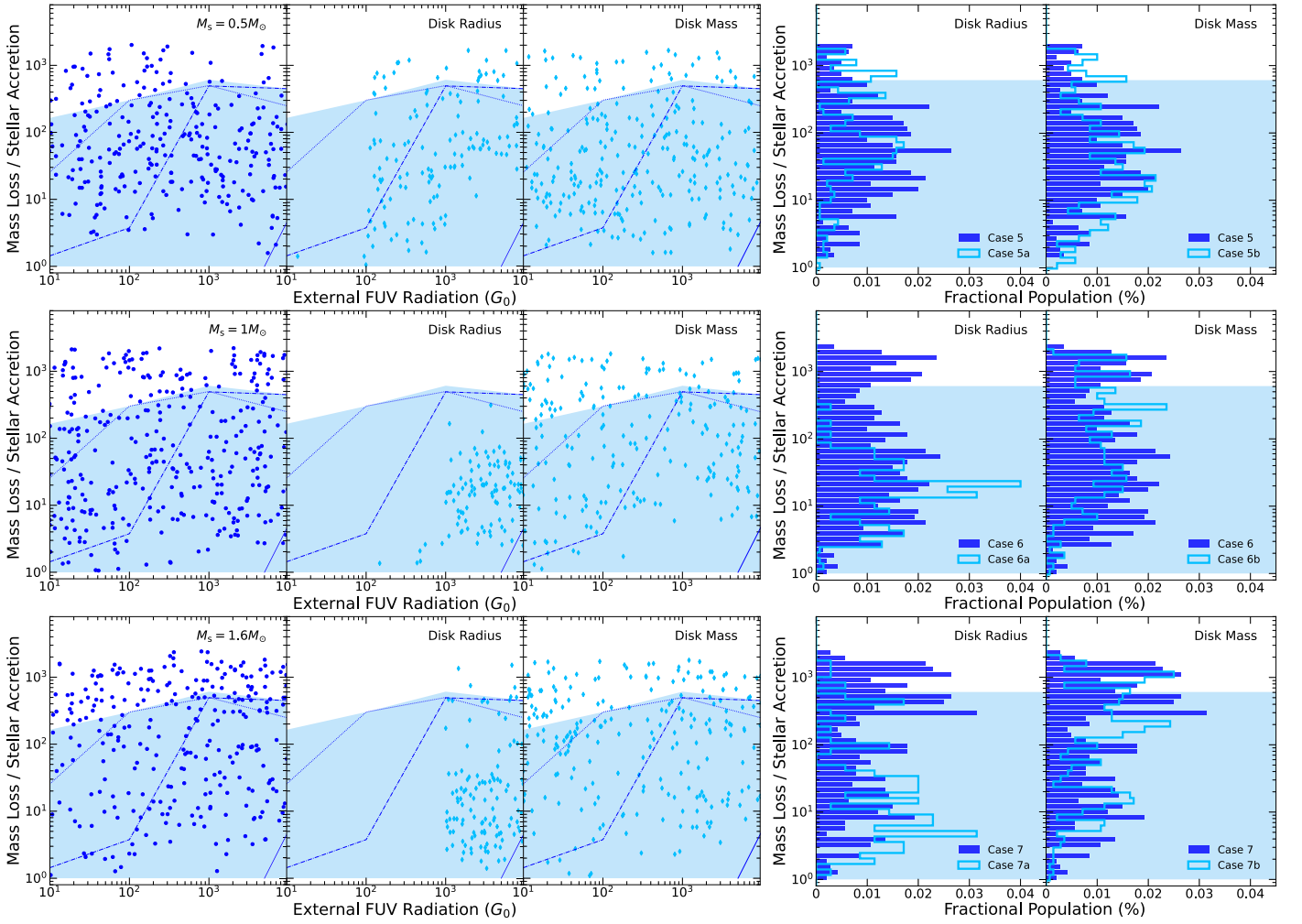


Figure 6. Disk populations for outer thermal winds. The populations are generated by the Monte-Carlo method (Table 3). The top panel shows the results for the case that $M_s = 0.5 M_\odot$, the middle one is for the case that $M_s = 1 M_\odot$, and the bottom is for the case that $M_s = 1.6 M_\odot$. In the left panel, the disk populations are distributed in the $\dot{M}_{\text{loss}}/\dot{M}_{\text{acc}}-F_{\text{FUV}}$ diagram. Both r_d and M_d vary in all the plots; compared with the left plot, the ranges of r_d and M_d shrink on the central and right plots, respectively. In the right panel, the fractional populations are shown, in order to examine the effect of the range of model parameters. As expected, the resulting disk populations are most sensitive to the disk radius. The blue shaded region is a good representative of disk populations for wide ranges of r_d and M_d .

In addition, we currently consider disks actively undergoing accretion. We therefore remove disks that have \dot{M}_{acc} smaller than $10^{-9} M_\odot \text{ yr}^{-1}$. In this parameter study, nine cases are examined in total (Table 3).

Cases 5, 5a, and 5b adopt that $M_s = 0.5 M_\odot$. Our results show that disk populations are most sensitive to the disk size; nearly the entire population disappears at $F_{\text{FUV}} \gtrsim 10^2 G_0$ when $r_d \leq 50 \text{ au}$ (Case 5a). This occurs because winds from such tiny disks are negligible. Disk population does not change very much even if the range of M_d varies (Case 5b).

Cases 6, 6a, and 6b consider that $M_s = 1 M_\odot$. As with the case that $M_s = 0.5 M_\odot$, r_d is the most sensitive parameter; for this case, disk population is distributed at $F_{\text{FUV}} \gtrsim 10^3 G_0$ due

to the higher gravitational potential of the host star (Case 6a); equivalently, higher F_{FUV} is needed to launch winds.

Finally, Cases 7, 7a, and 7b study that $M_s = 1.6 M_\odot$. We confirm a similar trend, while the disk radius dependence is comparable to the case that $M_s = 1 M_\odot$. In summary, the shaded region specified in Figure 3 serves as a good guide to constrain disk population for the EPE case, as well.

Figure 7 shows the synthesized results for the case that $M_s = 1 M_\odot$. It is clear that the shaded regions defined in Figure 3 well capture disk populations generated by the Monte-Carlo methods. Hence it is reasonable to consider that the parameter space constrained by our model serves as good reference for differentiating the origin of winds from protoplanetary disks.

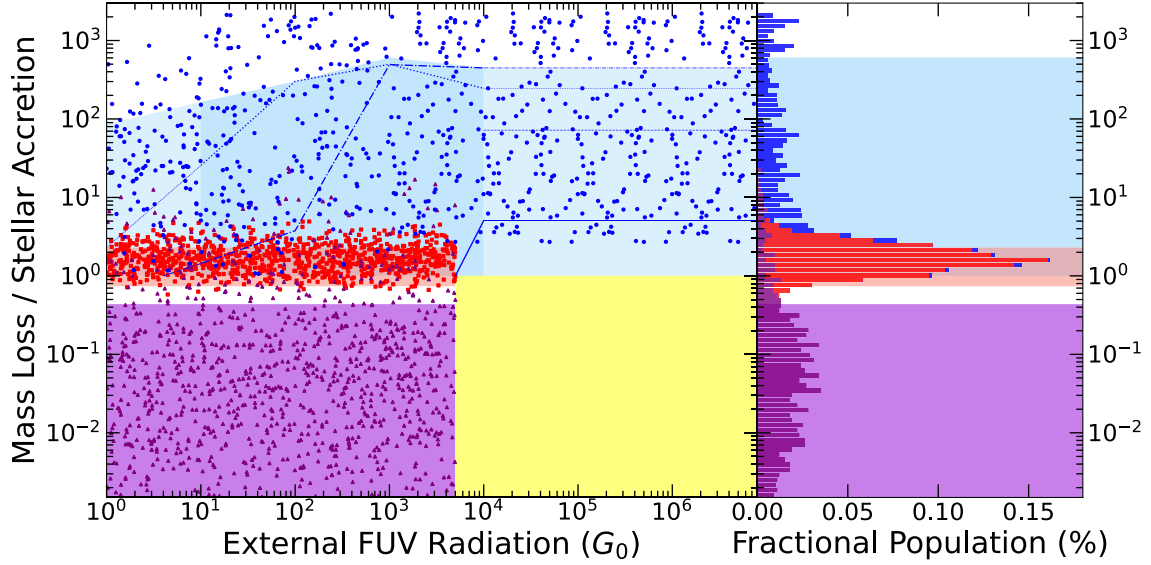


Figure 7. The synthesized results for the case that $M_s = 1 M_\odot$. The shaded regions well represent the disk populations produced by the Monte-Carlo method.

Appendix D

Estimating Inner Wind Mass Loss Rates for Observed Systems from [O I] 6300 Å

We here consider observed systems and estimate the mass loss rate that very likely originates from inner magnetic winds, using the forbidden [O I] 6300 Å emission line. Previous observations find strong evidence that the narrow/low-velocity component (LVC) of the [O I] 6300 Å emission traces the warm/hot neutral (atomic) layer of a slow, molecular/neutral disk wind launched from the inner part of protoplanetary disks (e.g., Natta et al. 2014; Simon et al. 2016; Whelan et al. 2021). We therefore focus on the component in the following analysis.

In principle, the wind mass loss rate ($\dot{M}_{\text{loss}}^{\text{in}}$) is estimated as

$$\dot{M}_{\text{loss}}^{\text{in}} \sim M_{\text{wind}} \frac{v_{\text{wind}}}{L_{\text{wind}}}, \quad (\text{D1})$$

where M_{wind} is the total mass carried away by winds, v_{wind} the wind velocity, and L_{wind} the physical extent occupied by the winds. Observations of the [O I] 6300 Å emission line provide its line flux and shape. Thus, one can estimate $\dot{M}_{\text{loss}}^{\text{in}}$ by converting these two observables to three physical quantities.

The quantity, v_{wind} , is a direct measurement of the velocity shift of the [O I] 6300 Å narrow-line component with respect to the system radial velocity. The quantities M_{wind} and L_{wind} are proportional to the total dereddened [O I] 6300 Å narrow-line component luminosity ($L[\text{O I}]$). We follow a simplified method outlined in Natta et al. (2014) to derive M_{wind} from $L[\text{O I}]$; a more elaborate method can be found elsewhere (e.g., Fang et al. 2018). More specifically, we use Equation (5) in Natta et al. (2014), assuming that $j([\text{O I}]6300) = 6.0 \times 10^{-16} \pm 5.0 \times 10^{-16} \text{ erg s}^{-1} \text{ O I}^{-1}$ and $\alpha(\text{O I}) = 5.0 \times 10^{-4} \pm 3.0 \times 10^{-5}$, where $j([\text{O I}]6300)$ is the line emissivity and $\alpha(\text{O I})$ is the fraction of the neutral gas wind made up of O I. Estimating L_{wind} is most unconstrained because it depends sensitively on the geometry of the winds. We here consider two different geometries, which may provide upper and lower bounds to the possible (realistic) ranges of L_{wind} . The first geometry of the winds is spherical symmetric. This is adopted in Natta et al. (2014) and leads to the most conservative estimate for L_{wind} , which gives a lower limit. The second geometry is a

Table 4

The Ratio of the Inner Wind Mass Loss Rate to the Stellar Accretion Rate for Observed Systems

Target Name	$F_{\text{FUV}}(G_0)$	$\dot{M}_{\text{loss}}^{\text{in}}/\dot{M}_{\text{acc}}$
CI Tau	26	0.016 ± 0.38
CW Tau	40	0.018 ± 0.61
DG Tau	25	0.099 ± 1.8
DL Tau	32	0.032 ± 0.75
DN Tau	4	0.26 ± 4.9
DR Tau	29	0.012 ± 0.31
GI Tau	41	0.063 ± 2.0
HN Tau	38	0.40 ± 7.4
HQ Tau	37	0.33 ± 6.2
Ex Lup	5	0.0041 ± 0.085
RU Lup	5	0.01808 ± 0.35
RY Lup	9	0.022 ± 0.54
Sz 73	9	0.29 ± 5.5
Sz 98	3	0.012 ± 0.27
Ass Cha T 2-3	2	0.18 ± 4.0
TW Cha	6	0.17 ± 3.9
CT Cha A	3	0.015 ± 0.37
Sz 22	6	0.0163 ± 0.38
VW Cha	3	0.11 ± 2.5
ESO H α 562	5	1.6 ± 35
Ass Cha T 2-38	5	0.15 ± 3.3
CHXR 79	7	5.5 ± 123
Ass Cha T 2-40	2	0.00021 ± 0.11
Sz 32	7	0.024 ± 0.56
Ass Cha T 2-44	1	0.0023 ± 0.054
Sz 37	7	0.042 ± 0.99
CHX 18N	7	0.099 ± 2.3
Ass Cha T 2-52	6	0.0074 ± 0.17
CW Cha	1	0.011 ± 0.27
CoKu Tau 4	48	7.9 ± 166
FZ Tau	61	0.015 ± 0.37

bipolar cone. By assuming that winds are launched from the innermost (~ 0.1 au) region of the disk, the resulting estimate of L_{wind} gives an upper limit. For both cases of geometry, the volumetric density of [O I] is calculated, using Equation (7) in Natta et al. (2014), and then this density is converted to L_{wind} ,

using the appropriate geometric conversion factor for these cases. We use the midpoint between the two geometries for L_{wind} in our estimates, with the end points (upper and lower limits from the conical and spherical geometries, respectively) constituting the 1σ errors on L_{wind} .

All errors in variables required to compute $\dot{M}_{\text{loss}}^{\text{in}}$ are assumed to be uncorrelated and therefore follow traditional error-propagation rules. To compute the ratio of $\dot{M}_{\text{loss}}^{\text{in}}$ to \dot{M}_{acc} and its error, we assume an order of magnitude error range on the measured accretion rates. Since it is very unlikely that simultaneous observations were conducted to determine both $\dot{M}_{\text{loss}}^{\text{in}}$ and \dot{M}_{acc} , it would be safest to apply this error range. We also assume that the measurements of $\dot{M}_{\text{loss}}^{\text{in}}$ and \dot{M}_{acc} are intrinsically correlated in nature, that is, it is expected that a higher \dot{M}_{acc} leads to a higher value of $\dot{M}_{\text{loss}}^{\text{in}}$. Therefore, we assume that errors associated with $\dot{M}_{\text{loss}}^{\text{in}}$ and \dot{M}_{acc} are correlated, and adopt error propagation for correlated variables.

Our estimates for observed systems are summarized in Table 4; the observed data needed to compute $\dot{M}_{\text{loss}}^{\text{in}}/\dot{M}_{\text{acc}}$ and its error are adapted from Simon et al. (2016), Nisini et al. (2018), and Gangi et al. (2020). The value of F_{FUV} is estimated as done in Appendix E.

Appendix E

Estimating Outer Wind Mass Loss Rates for Observed Systems

The outer wind mass loss rate ($\dot{M}_{\text{loss}}^{\text{out}}$) for observed systems can be estimated as (e.g., Johnstone et al. 1998)

$$\left(\frac{\dot{M}_{\text{loss}}^{\text{out}}}{10^{-8} M_{\odot} \text{ yr}^{-1}} \right) \simeq \left(\frac{R_{\text{LF}}}{1200 \text{ au}} \right)^{3/2} \left(\frac{d}{1 \text{ pc}} \right)^{-1} \left(\frac{\dot{N}_{\text{Ly}}}{10^{45} \text{ s}^{-1}} \right)^{1/2}, \quad (\text{E1})$$

where R_{LF} is the radius of the ionization front defined around the surface of a protoplanetary disk by the external ionizing source, d is the distance between the disk and the source, and \dot{N}_{Ly} is the extreme-UV photon count from the source. As done in Section 2.4, the disk accretion rate (\dot{M}_{acc}) onto the host star is estimated from the disk mass. Thus, the ratio of $\dot{M}_{\text{loss}}^{\text{out}}$ to \dot{M}_{acc} for observed systems is estimated from Equations (E1) and (10).

We also estimate the external FUV field (F_{FUV}) as

$$F_{\text{FUV}} = F_{\text{FUV}}(\text{at } 0.1 \text{ pc}) \left(\frac{d}{0.1 \text{ pc}} \right)^{-2}. \quad (\text{E2})$$

Our estimates for observed systems are summarized in Table 5. We obtained the observed data from Henney & Arthur (1998), Eisner et al. (2018), and Haworth et al. (2021) and conduct traditional error-propagation calculations to estimate errors. When errors of the data are not provided, we assume that errors of R_{LF} are $\pm 10\%$ of the observed value, errors of d are $\pm 50\%$ of the observed value, and errors of \dot{N}_{Ly} are ± 2 times the observed value.

Table 5

The Ratio of the Outer Wind Mass Loss Rate to the Stellar Accretion Rate for Observed Systems

Target Name	$F_{\text{FUV}}(10^5 G_0)$	$\dot{M}_{\text{loss}}^{\text{out}}/\dot{M}_{\text{acc}}$
NGC 2024 Proplyd 1 (VLA 1)	2.4	5.1 ± 6.7
NGC 2024 Proplyd 2 (VLA 4)	5.4	52 ± 63
NGC 2024 Proplyd 3 (VL A 20b)	5.5	35 ± 48
NGC 2024 Proplyd 4 (VL A 20a)	6.2	19 ± 24
NGC 2024 Candidate Proplyd 5	1.2	15 ± 20
NGC 2024 Candidate Proplyd 7	1.8	9.3 ± 11
ONC 152-319	3.1	$1.8 \times 10^2 \pm 2.7 \times 10^2$
ONC 154-324	8.2	$1.3 \times 10^2 \pm 5.6 \times 10^2$
ONC 155-338	2.8	27 ± 35
ONC 159-338	15	41 ± 59
ONC 159-350	5.4	15 ± 16
ONC 161-314	1.3	33 ± 63
ONC 161-328	40	$2.2 \times 10^2 \pm 2.9 \times 10^2$
ONC 166-316	24	$3.1 \times 10^2 \pm 2.4 \times 10^3$
ONC 168-328	27	40 ± 76
ONC 170-337	13	4.2 ± 17
ONC 171-340	6.4	$38 \pm 1.2 \times 10^2$
ONC 173-341	2.3	23 ± 53
ONC 177-341	5.3	$1.8 \times 10^2 \pm 4.9 \times 10^2$
ONC 180-331	5.4	$1.5 \times 10^2 \pm 3.3 \times 10^2$

ORCID iDs

Yasuhiro Hasegawa  <https://orcid.org/0000-0002-9017-3663>
 Thomas J. Haworth  <https://orcid.org/0000-0002-9593-7618>
 Keri Hoadley  <https://orcid.org/0000-0002-8636-3309>
 Jinyoung Serena Kim  <https://orcid.org/0000-0001-6072-9344>
 Neal J. Turner  <https://orcid.org/0000-0001-8292-1943>
 Ilaria Pascucci  <https://orcid.org/0000-0001-7962-1683>
 Erika T. Hamden  <https://orcid.org/0000-0002-3131-7372>

References

- Adams, F. C., Hollenbach, D., Laughlin, G., & Gorti, U. 2004, *ApJ*, **611**, 360
 Bai, X.-N. 2016, *ApJ*, **821**, 80
 Bai, X.-N. 2017, *ApJ*, **845**, 75
 Bai, X.-N., & Stone, J. M. 2013, *ApJ*, **769**, 76
 Bai, X.-N., Ye, J., Goodman, J., & Yuan, F. 2016, *ApJ*, **818**, 152
 Balbus, S. A., & Hawley, J. F. 1991, *ApJ*, **376**, 214
 Balbus, S. A., & Hawley, J. F. 1998, *RvMP*, **70**, 1
 Birnstiel, T., Klahr, H., & Ercolano, B. 2012, *A&A*, **539**, A148
 Chambers, J. E. 2016, *ApJ*, **825**, 63
 Clarke, C. J. 2007, *MNRAS*, **376**, 1350
 Concha-Ramírez, F., Wilhelm, M. J. C., Portegies Zwart, S., & Haworth, T. J. 2019, *MNRAS*, **490**, 5678
 de Valon, A., Dougados, C., Cabrit, S., et al. 2020, *A&A*, **634**, L12
 Eisner, J. A., Arce, H. G., Ballering, N. P., et al. 2018, *ApJ*, **860**, 77
 Ercolano, B., & Pascucci, I. 2017, *RSOS*, **4**, 170114
 Fang, M., Pascucci, I., Edwards, S., et al. 2018, *ApJ*, **868**, 28
 Ferreira, J., & Pelletier, G. 1995, *A&A*, **295**, 807
 Flaherty, K., Hughes, A. M., Simon, J. B., et al. 2020, *ApJ*, **895**, 109
 Gammie, C. F. 1996, *ApJ*, **457**, 355
 Gangi, M., Nisini, B., Antonucci, S., et al. 2020, *A&A*, **643**, A32
 Gressel, O., Ramsey, J. P., Brinch, C., et al. 2020, *ApJ*, **896**, 126
 Habing, H. J. 1968, *BAN*, **19**, 421
 Hartmann, L., Calvet, N., Gullbring, E., & D'Alessio, P. 1998, *ApJ*, **495**, 385
 Hartmann, L., Herczeg, G., & Calvet, N. 2016, *ARA&A*, **54**, 135
 Hasegawa, Y., Okuzumi, S., Flock, M., & Turner, N. J. 2017, *ApJ*, **845**, 31
 Hawley, J. F., Gammie, C. F., & Balbus, S. A. 1995, *ApJ*, **440**, 742
 Haworth, T. J., & Clarke, C. J. 2019, *MNRAS*, **485**, 3895

- Haworth, T. J., Clarke, C. J., Rahman, W., Winter, A. J., & Facchini, S. 2018, *MNRAS*, **481**, 452
- Haworth, T. J., Kim, J. S., Winter, A. J., et al. 2021, *MNRAS*, **501**, 3502
- Henney, W. J., & Arthur, S. J. 1998, *AJ*, **116**, 322
- Ida, S., Guillot, T., & Morbidelli, A. 2008, *ApJ*, **686**, 1292
- Johnstone, D., Hollenbach, D., & Bally, J. 1998, *ApJ*, **499**, 758
- Louvet, F., Dougados, C., Cabrit, S., et al. 2018, *A&A*, **618**, A120
- Lyra, W., & Umurhan, O. M. 2019, *PASP*, **131**, 072001
- Manara, C. F., Mordasini, C., Testi, L., et al. 2019, *A&A*, **631**, L2
- McNally, C. P., Nelson, R. P., Paardekooper, S.-J., & Benítez-Llambay, P. 2019, *MNRAS*, **484**, 728
- Miller, K. A., & Stone, J. M. 2000, *ApJ*, **534**, 398
- Natta, A., Testi, L., Alcalá, J. M., et al. 2014, *A&A*, **569**, A5
- Nisini, B., Antonucci, S., Alcalá, J. M., et al. 2018, *A&A*, **609**, A87
- Pascucci, I., Banzatti, A., Gorti, U., et al. 2020, *ApJ*, **903**, 78
- Richling, S., & Yorke, H. W. 2000, *ApJ*, **539**, 258
- Rosotti, G. P., Clarke, C. J., Manara, C. F., & Facchini, S. 2017, *MNRAS*, **468**, 1631
- Sano, T., & Inutsuka, S.-I. 2001, *ApJL*, **561**, L179
- Seifert, R. A., Cleeves, L. I., Adams, F. C., & Li, Z.-Y. 2021, *ApJ*, **912**, 136
- Shakura, N. I., & Sunyaev, R. A. 1973, *A&A*, **500**, 33
- Simon, M. N., Pascucci, I., Edwards, S., et al. 2016, *ApJ*, **831**, 169
- Speedie, J., Pudritz, R. E., Cridland, A. J., Meru, F., & Booth, R. A. 2021, *MNRAS*, **510**, 6059
- Suzuki, T. K., & Inutsuka, S.-I. 2009, *ApJL*, **691**, L49
- Suzuki, T. K., Muto, T., & Inutsuka, S.-I. 2010, *ApJ*, **718**, 1289
- Suzuki, T. K., Ogihara, M., Morbidelli, A., Crida, A., & Guillot, T. 2016, *A&A*, **596**, A74
- Turner, N. J., Fromang, S., Gammie, C., et al. 2014, in *Protostars and Planets VI*, ed. H. Beuther et al. (Tucson, AZ: Univ. Arizona Press), 411
- Wang, L., Bai, X.-N., & Goodman, J. 2019, *ApJ*, **874**, 90
- Wardle, M. 2007, *Ap&SS*, **311**, 35
- Whelan, E. T., Pascucci, I., Gorti, U., et al. 2021, *ApJ*, **913**, 43
- Williams, J. P., & Cieza, L. A. 2011, *ARA&A*, **49**, 67
- Winter, A. J., Ansdell, M., Haworth, T. J., & Kruijssen, J. M. D. 2020a, *MNRAS*, **497**, L40
- Winter, A. J., Kruijssen, J. M. D., Longmore, S. N., & Chevance, M. 2020b, *Natur*, **586**, 528